Estimating the Volume Transport of Kuroshio Extension Based on Satellite Altimetry and Hydrographic Data

HAIHONG GUO,[a,b,c] ZHAOHUI CHEN,[b,c] HAIYUAN YANG,[b,c] YU LONG,[d] RUICHEN ZHU,[b,c] YUEQI ZHANG,[b,c] ZHAO JING,[a,b,c] AND CHEN YANG[b,c]

[a] *Laoshan Laboratory, Qingdao, China*
[b] *Frontier Science Center for Deep Ocean Multi-spheres and Earth System, Ocean University of China, Qingdao, China*
[c] *Physical Oceanography Laboratory, Ocean University of China, Qingdao, China*
[d] *State Key Laboratory of Satellite Ocean Environment Dynamics, Second Institute of Oceanography, Ministry of Natural Resources, Hangzhou, China*

(Manuscript received 10 February 2023, in final form 26 May 2023, accepted 23 August 2023)

ABSTRACT: In this study, an effective method of estimating the volume transport of the Kuroshio Extension (KE) is proposed using surface geostrophic flow inferred from satellite altimetry and vertical stratification derived from climatological temperature/salinity (*T*/*S*) profiles. Based on velocity measurements by a subsurface mooring array across the KE, we found that the vertical structure of horizontal flow in this region is dominated by the barotropic and first baroclinic normal modes, which is commendably described by the leading mode of empirical orthogonal functions (EOFs) of the observed velocity profiles as well. Further analysis demonstrates that the projection coefficient of moored velocity onto the superimposed vertical normal mode can be represented by the surface geostrophic velocity as derived from satellite altimetry. Given this relationship, we proposed a dynamical method to estimate the volume transport across the KE jet, which is well verified with both ocean reanalysis and repeated hydrographic data. This finding implicates that, in the regions where the currents render quasi-barotropic structure, it takes only satellite altimetry observation and climatological *T*/*S* to estimate the volume transport across any section.

SIGNIFICANCE STATEMENT: The Kuroshio Extension (KE) plays an important role in the midlatitude North Pacific climate system. To better understand the KE dynamic and its influences, it is very important to estimate the KE transport. However, direct observation is very difficult in this area. Combining a subsurface mooring array and climatological temperature/salinity data, the vertical structure of the KE is explored in this study using mode decomposition methods. The relationship between the vertical structure of the zonal velocity and surface geostrophic flow observed by satellite altimetry in the KE region is further investigated. Based on this relationship, the KE transport can be well estimated by using satellite altimetry observation and historical hydrographic observation.

KEYWORDS: Mass fluxes/transport; Ocean circulation; Altimetry

1. Introduction

The Kuroshio, which originates from the Philippines coast and leaves Japan in the midlatitude ocean, acts as a mass, momentum, and heat conveyor connecting the tropical and extratropical northern Pacific Ocean. After leaving the western boundary, the Kuroshio veers eastward as an inertial jet, that is, the Kuroshio Extension (KE). This jet, known as the boundary between the subtropical gyre and the subpolar gyre of the northern Pacific, sets up a sharp potential vorticity front and a strong hydrologic front in the midlatitude North Pacific, resulting in distinct seawater chemistry and physical properties on both sides (Qiu 2003). Due to its high nonlinearity, abundant eddies shedding from KE through baroclinic/barotropic instabilities make it one of the most energetic regions in global oceans (Hurlburt et al. 1996; Yang and Liang 2018).

The KE plays an important role in modulating the environmental features from the surface to the deep layer (Bishop et al. 2012; Yang et al. 2021). In the surface layer, as a typical subtropical western boundary extension, the KE and surrounding waters are hotspots of marine heat waves with large sea surface temperature variability (Oliver et al. 2021). In the subsurface layer, the KE acts as a critical pathway of the North Pacific Intermediate Water (NPIW), characterized by a salinity minimum just below the warm/salty surface layer (Hiroe et al. 2002), which is an important route for carbon uptake from subarctic to subtropical regions (Tsunogai et al. 1993). Besides, the subducted vertically homogeneous water, known as the Subtropical Mode Water (STMW), carries a huge amount of water mass with "memory" away from the formation region in the KE and widely distributed toward the lower latitudes (Suga and Hanawa 1995). In the deep layer down to a great depth of 5000 m, evidence was found that the abyssal currents are weakly bottom intensified (Bishop et al. 2012). Hence, abundant multiscale oceanic processes of KE, either at the surface or deep down to the bottom, play an important role in energy transfer and mass transport, exerting essential impacts on local climate and ecosystem in the extratropical North Pacific (Qiu et al. 2007; Jayne et al. 2009; Kida et al. 2015; Ma et al. 2016).

To better understand the role of the Kuroshio in the climate system, it is necessary to first know the capacity of the

Corresponding author: Zhaohui Chen, chenzhaohui@ouc.edu.cn

DOI: 10.1175/JTECH-D-23-0018.1

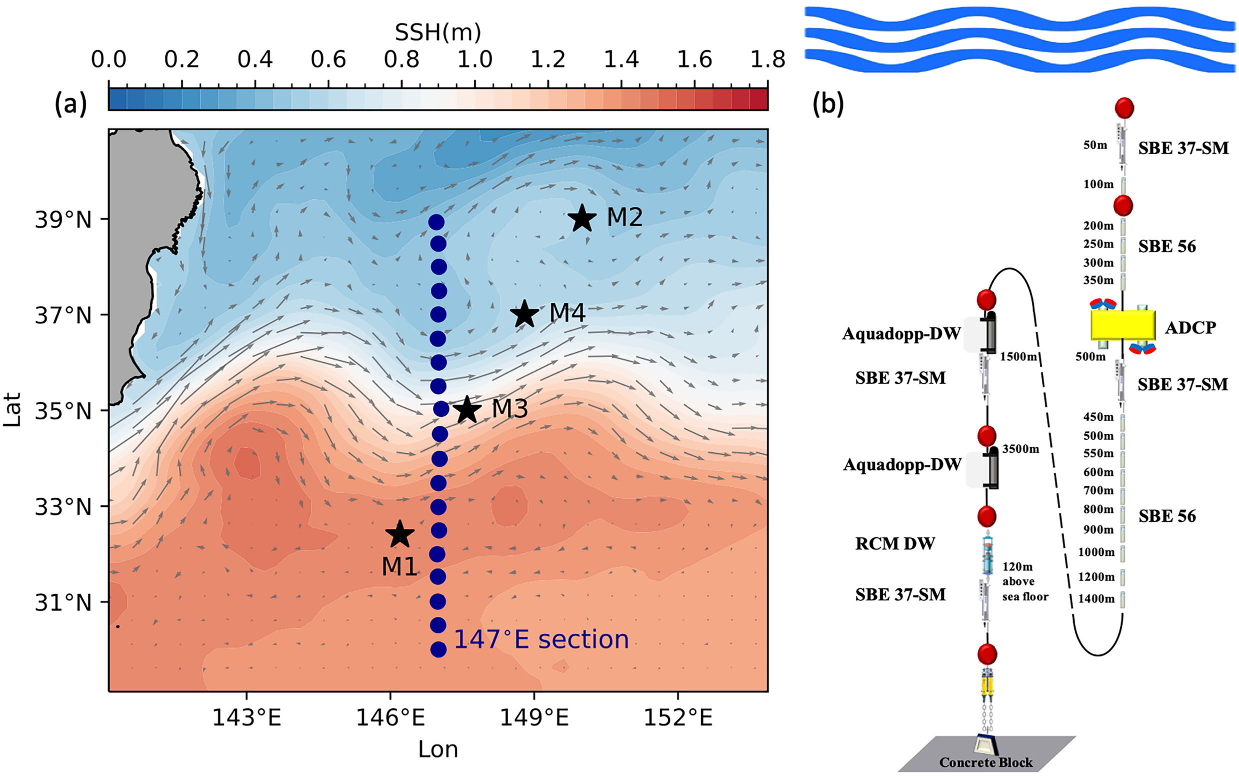

FIG. 1. (a) Locations of subsurface moorings (black stars). The blue dots denote a historical hydrographic section (147°E) used for comparison in this study. The color shading and gray arrows respectively represent the climatological sea surface height (SSH) and the surface geostrophic current derived from AVISO. (b) Schematic of the basic design of subsurface moorings of KEMS.

Kuroshio in transporting mass and heat along its pathway. Over the past several decades, there has been a growing body of observational efforts to estimate the Kuroshio transport by numerous hydrographic and current measurements, from east of the Philippine coast to east of the Taiwan Island, from the eastern China Sea (ECS) shelf break to the south of Japan. Despite the great challenges of long-term and sustainable in situ observations, there have been several efforts to measure the KE transport by multiple approaches. For example, Joyce (1987) estimated the eastward KE transport (56 ± 2 Sv) (1 Sv ≡ 10^6 m^3 s^{-1}) using hydrographic data occupied across the KE along 165°E. Hall (1989) directly measured the KE transport with a corresponding standard deviation 87 ± 21 Sv based on a single mooring with current meters. Yoshikawa et al. (2004) calculated transport of 163 Sv across 146°25′E and 113 Sv across 152°30′E using lowered ADCP data. Jayne et al. (2009) estimated a total downstream transport of 114 ± 13 Sv and a weaker Eulerian averaging transport of 79 Sv for the KE with systematic observations of the Kuroshio Extension System Study (KESS) project.

The above direct measurements of KE transport are, to some extent, temporally discontinuous and spatially discrete so that large deviations exist among different studies. Until very recently, direct and long-term observations of volume transport for this strong jet are still lacking, which is due to the complex structure of the strong current, as well as rich eddies and fronts in this region. Although Qiu (2003) has provided an acceptable and reasonable proxy of the KE strength, through which the time series of the KE transport can be indirectly derived in terms of sea surface height (SSH) difference across the KE jet, we are still facing challenges to obtain a decadal–multidecadal time series of the KE transport based on current observations. In this regard, we need to develop a practical approach to accurately estimate the KE transport given the insufficient in situ observations in this region to reduce the biases among observational and modeling studies.

To sustain long-term data collection in the KE region, China has initiated the Kuroshio Extension Mooring System (KEMS; https://cn-kems.net/) with an array of subsurface moorings across the KE jet since 2015 (Fig. 1, detailed information is provided in the following section). Different from the subsurface moorings that lasted for two years during the KESS project, the longest time duration of subsurface moorings of KEMS lasted for more than 6 years and continued until the last recovery. The maintenance of the subsurface mooring array can provide direct and long-term observations that cover the velocity from the upper ocean to some great depth across the KE jet, which is beneficial to set up a preliminary view of the circulation in the KE region.

It is noteworthy that limited subsurface moorings are sparsely deployed with over 200 km between each mooring, which makes it difficult to directly calculate the KE transport.

TABLE 1. Details of the instrument configuration for the moorings.

Instrument	Type	Quantities	Sampling interval	Nominal depth	Data retrieval failure
ADCP	Workhorse Long Ranger ADCP	2	1 h	400/500 m	M1 (2017–18; 2021–22)
CM	Aquadopp DW/Seaguard RCM DW	3	30 min	1500, 3500, and 5500 m	M3 5500 m (2018–19; 2020–21); M4 5500 m (2020–21)
CTD	SBE 37-SM MicroCAT C-T (P) recorder	4	5 min	100, 400, 1500, and 5500 m	M1 100 m and M1 400 m (2021–22); M3 100 m (2017–18); M4 100 m (2020–22); M4 400 m (2021–22)
T chain	SBE 56 temperature logger	15	1 min	100/150–1000/1500 m	M1 (2017–18; 2021–22)

In this paper, our main purpose is to explore the dynamical relationship between the vertical structure of the observed velocity and the surface geostrophic flow by combining climatological, hydrographic data and altimetry data. Subsequently, an effective method is proposed to calculate the KE transport based on this relationship. The paper is organized as follows: Data and methods are first described in section 2, followed by presenting the results of the vertical structure and its relevance with the geostrophic flow in section 3. Then the volume transport estimation and verification are presented in section 4. We summarize the results in section 5.

2. Data

a. Mooring data

As part of KEMS, five subsurface moorings have successively been deployed along a line crossing the axis of KE since late 2015. Following the last recovery in July 2022, there are currently four subsurface moorings (M1, M2, M3, and M4) on site, which range from 32.4°N, 146.2°E in the subtropical region to 39.0°N, 150.0°E in the Kuroshio–Oyashio mixed zone. As shown in Fig. 1a, the climatological KE crosses the mooring array with mooring M3 being exactly located at the axis of the jet. The subsurface moorings are basically designed as follows: two ADCPs (RDI Workhorse Long Ranger 75 kHz) with one looking upward and the other downward are mounted on a main floating body at the nominal depth of 400/500 m; four CTDs (SBE 37-SM), three single-point current meters (Aquadopp DW/Seaguard RCM), and a chain of temperature loggers (SeaBird56) are equipped at the respective nominal depth of the subsurface mooring (Fig. 1b). More details about the mooring configuration are described in Table 1. Until the last recovery, the longest-running mooring, M1, has been maintained for almost 7 years despite some missing data due to equipment damage or the main floating body being broken away. Even the shortest-running mooring, M4, has lasted for over 2 years. Therefore, the multiyear accumulation of in situ current temperature/salinity (T/S) data used in this study is capable of providing sufficient information about the basic view of the KE jet and surrounding waters.

The ADCPs deployed on our moorings possess a maximum range of approximately 600 m. After data quality control, the combination of two ADCPs can provide reliable velocity measurements for the upper 1000 m. The sampling interval and vertical bin size of ADCPs were set to 1 h and 16 m, respectively. To accommodate the subsequent analysis with climatological T/S data, the moored velocities were then interpolated vertically at a standard depth with 10-m intervals combining two ADCPs and three single-point current meters. The sampling intervals of the temperature chain, CTDs, and current meters are 1, 5, and 30 min, respectively. All instrumental data were filtered with a cutoff period of 2 days (the local inertial period is ~22 h) to remove tidal effects and other high-frequency motions such as inertial gravity waves. More details about the data quality control are referred to Zhu et al. (2021).

b. Other datasets

To facilitate generating the time series of estimated volume transport, the gridded daily altimeter data with a spatial resolution of 1/4° from Archiving, Validation, and Interpretation of Satellite Oceanographic Data (AVISO) (https://www.aviso.altimetry.fr/) were used to provide the absolute surface geostrophic current for almost three decades (Ducet et al. 2000). The AVISO dataset started in 1993 and has been updated to the present, which offers gridded maps of sea surface heights and related variables across the world's oceans using altimeter measurements. These maps are generated through optimal interpolation, which combines long-track measurements from various altimeter missions. Bilinear interpolation is used to calculate the surface geostrophic current at the mooring site. The first baroclinic Rossby deformation radius in the KE region is approximately 40 km (Chelton et al. 1998; Ji et al. 2018), which is larger than the resolution of the AVISO data (0.25°). Nevertheless, despite the complexity of the region, the typical size of eddies in the KE area is large enough to span at least four points of the AVISO data. Therefore, this can provide a reasonable interpolation.

To explore the vertical structure of the KE, the monthly climatological *World Ocean Atlas 2018* (*WOA18*) temperature and salinity were used to perform vertical mode decomposition analysis. The *WOA18* is capable of providing objective analyses of climatologies that offer interpolated mean fields for oceanographic variables at standard depth levels across the world's oceans. The dataset utilizes decades of averaged *WOA18* collections (1955–2017) and has a horizontal resolution of 0.25° (Locarnini et al. 2019; Zweng et al. 2019). The stratification used for the decomposition was calculated by using the *WOA18 T/S* profiles located within a 0.5°-radius circle of the mooring site and the monthly climatological *T/S* data were interpolated into the daily field to accommodate the sampling frequency of mooring observations. It should be noted that *WOA18* only provides monthly climatological *T/S* profiles in the upper 1500 m. Therefore, the profiles below 1500 m were replaced by the respective climatological values, which exert very little influence on the shape of derived normal modes. It is worth noting that both the AVISO and *WOA18* datasets have a spatial resolution of 0.25°, which may not be adequate to capture small-scale phenomena such as submesoscale eddies. Nevertheless, since our research is mainly concerned with large-scale variations, using these datasets is justifiable.

We also used the eddy-resolving simulations of the Oceanic General Circulation Model for the Earth Simulator (OFES) to further validate the dynamical linkage between surface geostrophic flow and vertical structure of horizontal velocities. The OFES is based on the third version of the Modular Ocean Model (MOM3), with the computational domain of the OFES covering a near-global region extending from 75°S to 75°N, excluding the Arctic Ocean. The model employs a horizontal grid spacing of 1/10° and has 54 vertical levels. The distance between these levels varies from 5 m at the surface to a maximum depth of 6065 m with a spacing of 330 m (Masumoto et al. 2004). The OFES was spun up for 50 years and integrated forward from 1950 using daily surface forcing of the National Centers for Environmental Prediction/National Center for Atmospheric Research (NCEP–NCAR) reanalysis product (Kalnay et al. 1996). In this study, we only used the OFES data after 1993 to match up with the time span of AVISO data. In addition to model simulation data, we also calculated the KE transport based on geostrophic velocity derived from hydrographic data along the 147°E section to verify the applicability of the method proposed in this study (Long et al. 2018, 2019).

3. Observed versus reconstructed horizontal velocity

In this section, we first employed the vertical normal mode and EOF decompositions to investigate the vertical structure of horizontal velocity at M1, followed by the exploration of the relationship between two decompositions. A superimposed vertical normal mode was deduced to connect these two decompositions. Then we extended this relationship to other mooring sites.

a. Vertical normal mode decomposition

To investigate the vertical structure of horizontal flow in the KE region, we first employed vertical normal mode decomposition with respect to the mooring-observed velocities. In the linearized hydrostatic equations, the vertical components of the horizontal velocity $\mathbf{v}$ and the pressure field p in terms of an eigenfunction can be projected onto the complete orthogonal basis (Vallis 2017) that satisfies

$$\frac{d}{dz}\left[\frac{1}{N^2}\frac{dC_n(z)}{dz}\right] + \frac{1}{c_n^2}C_n(z) = 0 \quad \text{and} \tag{1a}$$

$$\frac{d}{dz}C_n(0) = -\frac{d}{dz}C_n(-H) = 0, \tag{1b}$$

where C_n are the orthogonal basis, c_n are the eigenspeeds, and N is the buoyancy frequency associated with the mean background stratification. The projected intensity of each mode on the horizontal velocity $\mathbf{v}(z, t)$ is determined by

$$\mathbf{P}_n(t) = \frac{\int_H^0 \mathbf{v}(z, t)C_n(z)\,dz}{\int_H^0 C_n^2(z)\,dz}, \tag{2a}$$

$$\mathbf{v}_n(z, t) = C_n(z)\mathbf{P}_n(t), \tag{2b}$$

where $\mathbf{P}_n(t)$ is the projection coefficient of each mode, representing the weight of the observed velocity projected onto each mode, and $\mathbf{v}_n(z, t)$ is the mode-n velocity of the nth baroclinic mode (Ma et al. 2022). The explained contribution of each mode can be calculated by the variance ratio between the decomposition-derived velocity and observed velocity.

Here we first focus on M1, the southernmost mooring that frequently experiences eddies passing by, to examine the horizontal velocity reconstructed by the vertical normal mode decomposition. Before exploring the vertical modes and their variability, it is necessary to provide an overview of the observed velocity. Figures 2a and 2b show the depth–time plots of the observed daily mean horizontal velocity at M1. The flow is mainly located in the upper 1500 m and the maximum velocity reaches up to 1.0 m s^{-1} near the surface, which is associated with the passage of intense eddies. We then applied the vertical normal mode decomposition to the observed velocity based on *WOA18* data using Eq. (1) and project the horizontal velocity onto the derived vertical modes using Eq. (2). As shown in Figs. 2c and 2d, the vertical structure of the horizontal velocity can be well represented by the barotropic mode and first baroclinic mode. The depth-independent barotropic mode explains 25% of the total variance, while the surface-intensified first baroclinic mode (Fig. 3a) explains 57% of the total variance. These two modes take up over 80% of the total variance (Table 2). The differences between the moored velocity and the sum of the first two modes are relatively small compared to the full velocity (Figs. 2e,f).

Although the reconstructed horizontal velocity is generally identical to the observed one in terms of strength, variability, and vertical structure (Fig. 2), it is not exactly always consistent with the observed velocity during some periods (e.g., February and May 2020). A detailed check showed that these differences are due to nonlocal generated eddies that originated far away from the mooring site (Fig. A1 in appendix A). These eddies trapped water masses from other regions, particularly the subpolar or mixed region between the Kuroshio and the Oyashio (Qiu and Chen 2005; Itoh and Yasuda 2010), and remote water masses with distinct *T/S* signals took over at the mooring site, altering the local stratification and thus the projection coefficient. Even so, the reconstructed horizontal velocity matches well with the mooring-observed velocity with

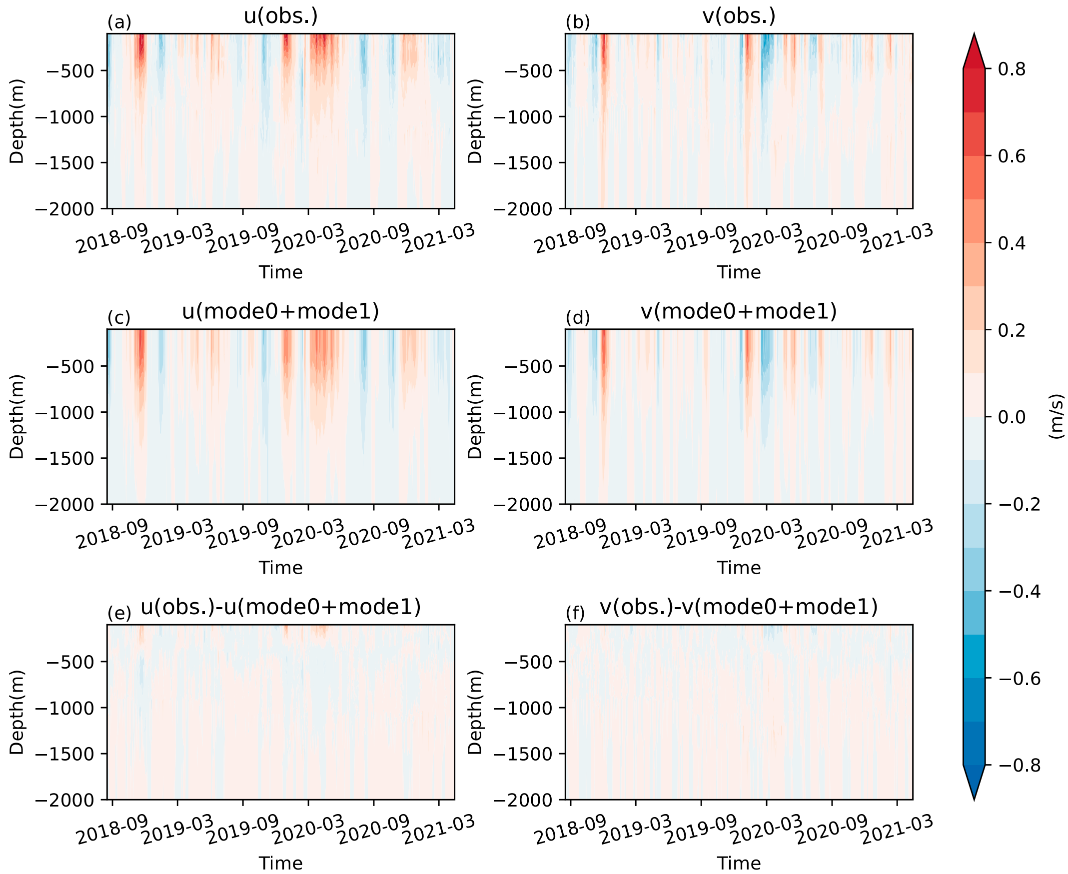

FIG. 2. Mooring-observed (a) zonal velocity and (b) meridional velocity at M1, and reconstructed (c) zonal and (d) meridional velocity based on the sum of velocity projected onto the barotropic and first baroclinic modes. Also shown is the difference between the observation and reconstruction of (e) zonal and (f) meridional velocity.

correlation coefficients ranging from 0.79 to 0.99 above 95% significance at different depths (Fig. 3b). Additionally, the differences between the observed and reconstructed velocity, as measured by the root-mean-square (RMS), are relatively small in comparison to the amplitude of the observed velocity (Figs. 3c,d). The largest RMS differences tend to occur near the surface. Specifically, the ratio of the RMS difference to the velocity amplitude for u ranges from 2% to 13% at different depths, while they range from 1% to 9% for v. We can confidently suggest that the barotropic and first baroclinic modes dominate the variability of horizontal velocity at M1. We also replaced the temperature from *WOA18* with observed values from the T chain of the mooring and conduct the same procedures, and the vertical mode is found to be quite similar (Fig. B1 in appendix B). Considering that the vertical mode decomposition will be applied to other regions where observed T profiles may not be available, it is more practical to keep using *WOA18* data in the following analysis.

b. EOF modes

To better understand the vertical structure of the horizontal velocity and how different vertical modes contribute, we used empirical orthogonal functions (EOFs) analysis to extract the dominant vertical structure of the observed full-depth horizontal velocity (Hannachi et al. 2007). It should be noted that before conducting EOF decomposition, the time-mean velocity at each depth from mooring observation was removed to highlight the variability of the velocity. Unlike the normal mode decomposition, EOF requires no additional hydrographic input like T/S. However, the principal EOF mode usually contains a mixing of different vertical normal modes (Ren et al. 2018). In this way, it is much easier to relate the EOF principal component (PC) with the geostrophic flow, which is the dominant part of the observed flow in this region (Uchida et al. 1998; Ji et al. 2018).

Figure 4a shows the first EOF mode (EOF1) of the horizontal velocity at M1 and its principal component (PC1). The EOF1 of both zonal and meridional velocities explains over 80% of the total variance of observed velocity, which is analogous to the first two vertical normal modes (Table 2). We compared the temporal variability of the surface geostrophic velocity with projection coefficients of EOF1 and superimposed normal modes, and the correlations among them are quite close (Figs. 4b,c, Table 2).

The explained variance shows that the EOF1 contains a mix of multimodes, which is not surprising since EOF

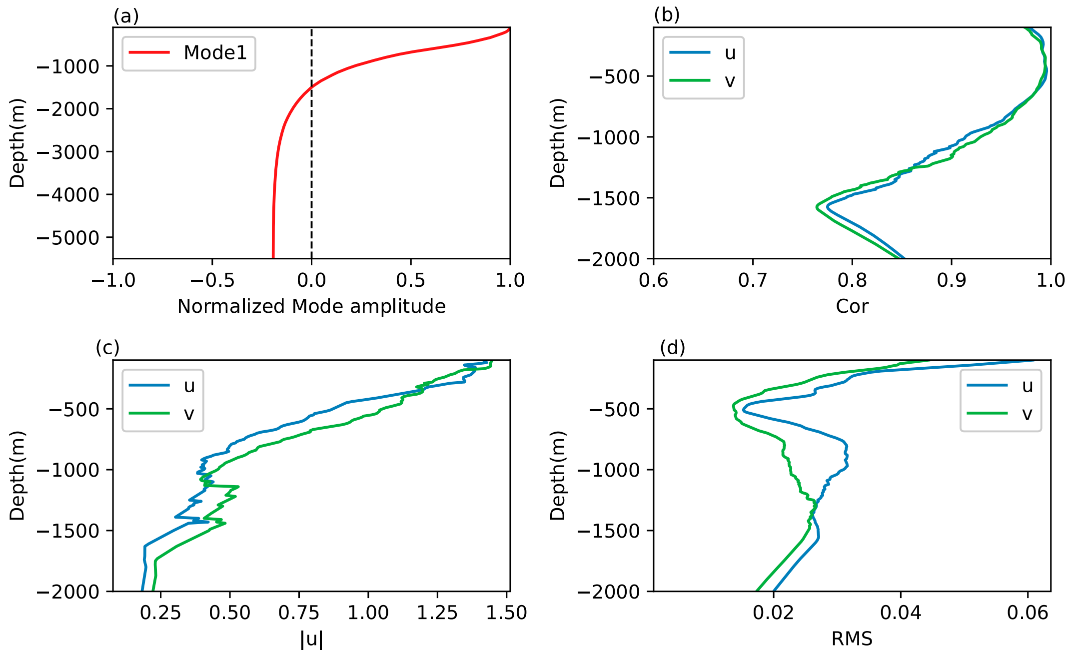

FIG. 3. (a) Vertical structure of the first baroclinic mode derived from *WOA18*. (b) Vertical distribution of correlation between observed and reconstructed velocity; all of the correlations are above 95% significance. (c) The amplitude of observed horizontal velocity at each depth. (d) The root-mean-square difference between observed and reconstructed velocity at each depth.

analysis is a purely statistical method while vertical normal mode decomposition involves diverse modes as hydrographic information is considered. However, on the one hand, each vertical normal mode [$C_n(z)$] corresponds to an independent time series [$\mathbf{P}_n(t)$ in Eq. (2a)], which makes it difficult to connect with the surface geostrophic flow. On the other hand, the EOF mode is highly dependent on the data input from in situ observations, which is impossible to estimate the vertical structure of the flow in other nonmooring regions. In this case, we need to relate the two independent methods of different principles to establish the statistical basis of the reconstruction of observed velocity.

c. *Mixed vertical modes*

As shown in Figs. 3a and 4a, both the first baroclinic mode and the EOF1 mode are characterized by surface intensification. The difference between these two modes is that the first baroclinic mode reverses its sign in the deep ocean, while the EOF1 remains in phase over the full depth. The zero-approaching flow in the deep ocean is achieved by adding the barotropic mode, which tends to weaken the deep layer flow and strengthen the upper layer flow, given that the barotropic mode is vertically uniform. Although the first baroclinic mode dominates the vertical structure in most parts of the world oceans (Chelton et al. 1998), it may underestimate the full velocity reconstruction using this single mode only in the KE region, since the barotropic

TABLE 2. The ratio between the intensity of the barotropic and first baroclinic modes, the explained variance of the superimposed vertical mode and EOF1 mode, the correlations (above 95% significance) between the AVISO-derived geostrophic velocity and these two modes [PC1 and $\mathbf{P}_s(t)$] for all mooring sites, the RMS difference between geostrophic velocity and $\mathbf{P}_s(t)$, the amplitude of the geostrophic velocity (AMP), and the ratio between RMS and AMP.

	M1 (32.4°N)		M3 (35°N)		M4 (37°N)		M2 (39°N)	
	u_g	v_g	u_g	v_g	u_g	v_g	u_g	v_g
r_c	0.196		0.201		0.231		0.259	
Var [$C_s(z)$]	88%	89%	80%	94%	89%	85%	87%	82%
Var (PC1)	91%	81%	85%	87%	78%	76%	86%	82%
Cor [u_g, $\mathbf{P}_s(t)$]	0.91	0.87	0.88	0.65	0.77	0.85	0.88	0.80
Cor (u_g, PC1)	0.90	0.87	0.87	0.66	0.78	0.84	0.81	0.78
RMS [u_g, $\mathbf{P}_s(t)$] (m s^{-1})	0.18	0.13	0.38	0.39	0.16	0.24	0.11	0.11
AMP (m s^{-1})	1.48	1.43	2.72	2.50	1.71	1.86	1.40	1.29
R (RMS/AMP)	12%	9%	14%	16%	10%	13%	8%	8%

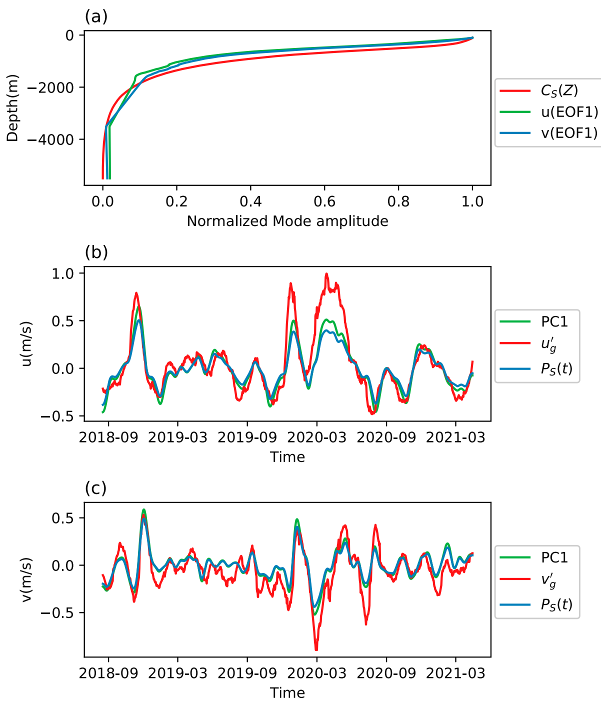

FIG. 4. (a) Normalized vertical structure of EOF1 (green line for u, and blue line for v) and superimposed barotropic and first baroclinic normal mode (C_s; red line) at M1. (b) Projection coefficients of the observed zonal velocity onto EOF1 (green line) and the superimposed vertical normal mode (blue line). The time series of the surface zonal geostrophic velocity at M1 is shown by the red line. (c) As in (b), but for the meridional velocity.

mode could explain the total variance of over 25%. Therefore, for the horizontal flow observed at M1, the vertical structure derived from EOF1 can be roughly regarded as the weighted sum of barotropic and first baroclinic modes. Both the first EOF1 and the sum of the first two vertical normal modes demonstrate a significantly weaker bottom flow in comparison to the upper layer flow (Fig. 4). This suggests that the barotropic and first baroclinic modes tend to counterbalance each other in the deep ocean. Therefore, for the upper layer flow, the primary characteristic can be represented by either the EOF1 or the sum of the barotropic and first baroclinic modes.

To combine the two barotropic and first baroclinic modes, we further explore their connections. The amplitude ratio between the projection coefficients of these two modes [$|\mathbf{P}_0(t)|/|\mathbf{P}_1(t)|$] is 0.21, and the correlations between $\mathbf{P}_0(t)$ and $\mathbf{P}_1(t)$ are 0.85 and 0.70 for the zonal and meridional velocities, respectively. The ratio between orthogonal basis of two modes at the bottom [$r_c = |C_1(H)|/|C_0(H)|$] is around 0.20, and the two modes are oriented in opposite directions [i.e., $C_0(H) \times C_1(H) < 0$]. Therefore, the barotropic and first baroclinic components tend to cancel each other out at the bottom. Based on this relationship, we can utilize the zero-velocity condition at the bottom to combine the barotropic and first baroclinic modes. The weight ratio between these two mode modes could be chosen as r_c, which can be obtained from the orthogonal basis. Considering that the barotropic mode is depth independent, we can linearly add it up with the first baroclinic mode by taking a weight of r_c,

$$C_s(z) = C_1(z) + r_c C_0(z). \tag{3}$$

Finally, we have obtained a superimposed mode, $C_s(z)$, that combines the first two vertical normal modes. To better reveal its relationship with EOF1, we normalized them to 1 at the surface as well. Figure 4a shows the vertical profile of these two modes, whose vertical structures are nearly identical to each other both for u and v. In this sense, in addition to EOF, we are able to reconstruct the main vertical structure of the horizontal flow at M1 via mixed vertical modes. It should be noted that using only two vertical normal modes can capture over 80% of the variance in the full vertical profile field and the residual differences are likely due to the higher baroclinic modes.

The projection coefficients [PC1, $\mathbf{P}_s(t)$] of the two modes [EOF1 and $C_s(z)$] are analogs to each other (Figs. 4b,c), so it is straightforward to reproduce the PC1 time series by linearly combing the barotropic and first baroclinic vertical normal modes. Given that both the EOF1 and $C_s(z)$ were normalized to 1 at the surface, their projection coefficients are equivalent to the surface flow. In the KE region, the low-frequency large-scale circulation is essentially in geostrophic balance, so that the surface geostrophic flow can be easily derived from SSH observed by satellite. Figures 4b and 4c show the time series of surface geostrophic flow anomaly (u'_g and v'_g) and the projection coefficients of the two modes. The correlations between the projection coefficients [$\mathbf{P}_s(t)$ and PC1] and u'_g are 0.91 and 0.90, respectively, and between [$\mathbf{P}_s(t)$ and PC1]u'_g and v'_g are 0.87 and 0.87, respectively, above 95% significance (Table 2). Therefore, it is reasonable to approximate the projection coefficients using the surface geostrophic flow.

d. Other mooring sites

The good relationship between vertical normal modes and EOF mode provides a practical approach to reconstructing the vertical structure of horizontal velocity by satellite altimetry and climatological T/S in the KE region. To estimate the KE transport more representatively, it is quite essential to extend this relationship to other moorings following the same procedure regarding M1. The zero crossing of the first baroclinic mode is shown to deepen at high latitudes at approximately 1500 (M1), 1630 (M3), 1750 (M4), and 1800 (M2) m. Based on this depth, the ocean can be dynamically divided into two layers, where the ocean above (below) the zero crossing is treated as the upper (lower) layer. This can be physically interpreted as gradually weaker stratification and a resultant larger vertical extent of the upper layer, which is mainly due to the decreasing temperature in the upper ocean with increasing latitude. Consequently, the flow at high latitudes tends to be more barotropic and the ratio between the barotropic and first baroclinic modes (r_c) increases as well (Table 2). Although the vertical structure of horizontal velocity varies along with increasing latitude, the superimposed

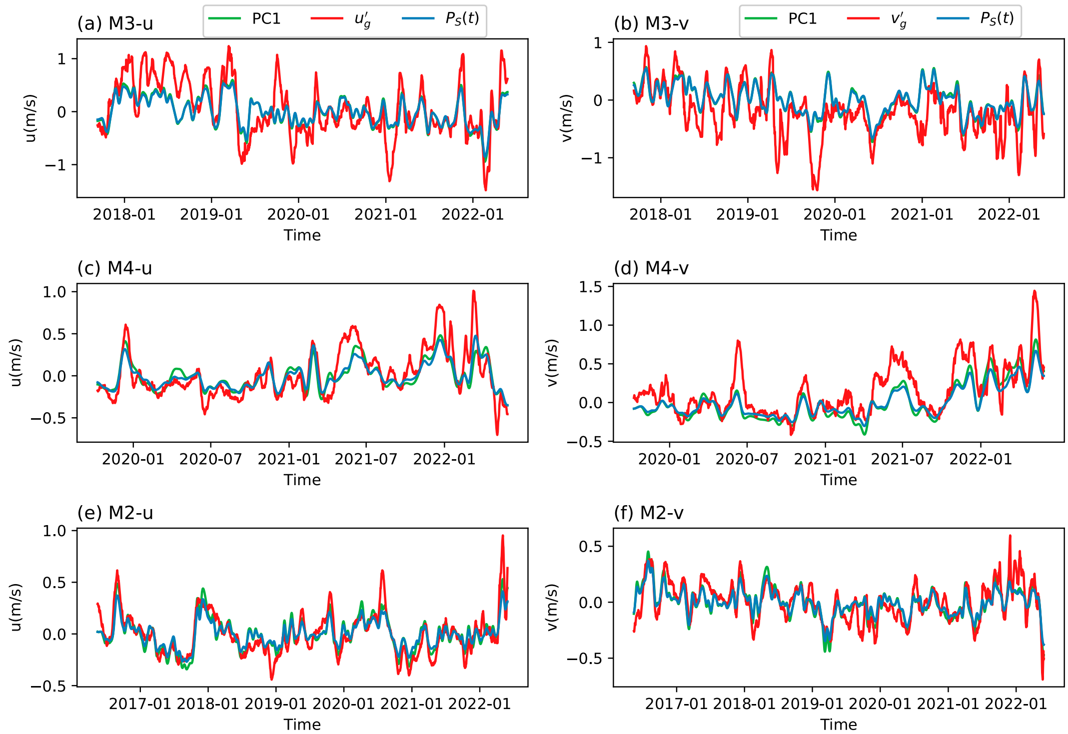

FIG. 5. As in Figs. 4b and 4c, but for M3, M4, and M2.

vertical mode and the EOF1 mode can reproduce the main vertical structure at every mooring.

At other moorings, the vertical structure and projection coefficients show similar results as M1 (Fig. 5). The correlations between u'_g or v'_g and the projection coefficients are over 0.6 above 95% significance for all moorings. Therefore, the dynamical relationship between two mode decomposition methods holds for all moorings. Based on this relationship, the vertical profile of the horizontal velocity across the KE jet can be well reconstructed, and the KE transport across any given section can be well estimated only by adopting satellite altimetry and climatological *T*/*S* profiles.

Note that the projection coefficients differ slightly from the surface geostrophic velocity at M3, due to its location on the Kuroshio axis where the front is strongest, and the water properties differ significantly between the two sides of the axis. The swing of the Kuroshio axis can disrupt the local decomposition, causing differences between the projection coefficients and the surface geostrophic velocities. These differences are relatively small compared to the amplitude of the geostrophic velocity, ranging from 8% to 16% (Table 2). Therefore, the nonlocal eddy or the swing KE axis may introduce around 10% uncertainty in the reconstructed velocity at a single mooring site. However, this discrepancy is unlikely to significantly impact the KE transport estimation. For the swing-axis effect, since we chose a line that crosses the axis, the uncertainty at different positions tends to cancel each other out. As for the nonlocal eddy effect, the uncertainty will decrease, considering the low-frequency variabilities.

4. Verification and application in volume transport estimation

a. Vertical structure of KE in OFES

The four moorings are too sparsely located to fully cover the KE jet, so it is necessary to examine the relationship and extend the reconstructed method to any other position. However, it is challenging to extrapolate this relationship to other regions without mooring data. To validate our approach, we employed reanalysis data from the OFES data to confirm the consistency between the reconstructed velocity and the full velocity. We first applied this method at M1 and find that the vertical structure and the temporal variability exhibit high similarity between the two projection coefficients (Fig. 6). It is worth noting that the performance of mode decomposition in the OFES is better than that of in situ observations based on the climatological *WOA18* data because the time-dependent hydrographic data in OFES can provide more compatible stratification. Therefore, we compute the dynamical modes at each time step, which, to the utmost extent, eliminates the effect from propagating eddies from other regions. Despite the improvement, there still exist some peaks with obvious inconsistency between surface geostrophic flow and projection coefficients (Figs. 6b,c), which is largely related to the role of nonlinearity and nonnegligible centrifugal force (Zhu et al. 2021). These processes will break the geostrophic balance, especially for strong currents. Nonetheless, the general features were well reproduced by the reconstructed method, and the correlation between surface geostrophic flow and $\mathbf{P}_s(t)$ of 0.91 for u and of 0.94 for v and the correlation

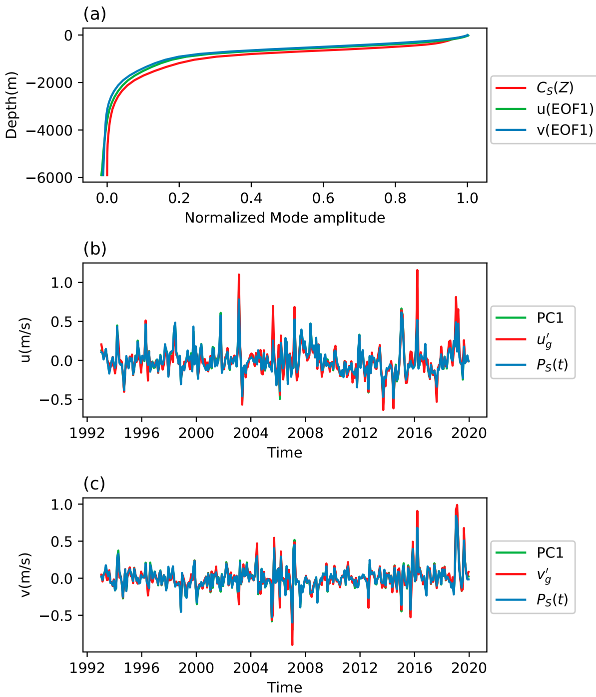

FIG. 6. As in Fig. 4, but for the analysis of OFES data.

between surface geostrophic flow and PC1 of 0.94 for u and of 0.97 for v all remain high, above 95% significance. The results at other moorings are essentially the same as the M1 (Fig. 7), which confirms this relationship at these positions.

Based on the verified relationship between geostrophic flow and reconstructed flow, we further calculate the KE transport across any selected section, since the OFES provides modeled velocity to directly obtain the volume transport, while SSH and T/S help to estimate the volume transport using constructed flow. Here, we selected the same section along the mooring array spanning from M1 to M2 across the KE jet (recall Fig. 1), we first reconstructed the horizontal velocity using the hydrographic data and SSH data from OFES from M1 to M2. Then we calculated the cross-sectional volume transport based on the model-output velocity and the reconstructed velocity, respectively. It is demonstrated in Fig. 8 that the volume transport estimated by the reconstructed method is quite consistent with OFES model transport in terms of either strength or variability. The model output transport has an average of 58.3 ± 11.9 Sv, with a corresponding standard deviation. In comparison, the estimated transport is 54.7 ± 14.4 Sv, indicating a slightly lower mean value and a higher variability. The RMS difference between the two transport methods is relatively small, at 11.4 Sv. Considering that the reconstructed velocity could be affected by nonlocal eddies characterized by short periods, this method loses adaptability for high-frequency variabilities. To further investigate the uncertainties, we conducted an analysis of the RMS difference on different time scales. The results indicate that the RMS differences are 10.1, 4.6, and 1.9 Sv for seasonal and higher frequencies, interannual, and decadal time scales, respectively. This suggests that the high-frequency variabilities, possibly due to nonlocal eddies, are the dominant source of the RMS difference. Additionally, the amplitude of the model transport, at 59.1 Sv, is

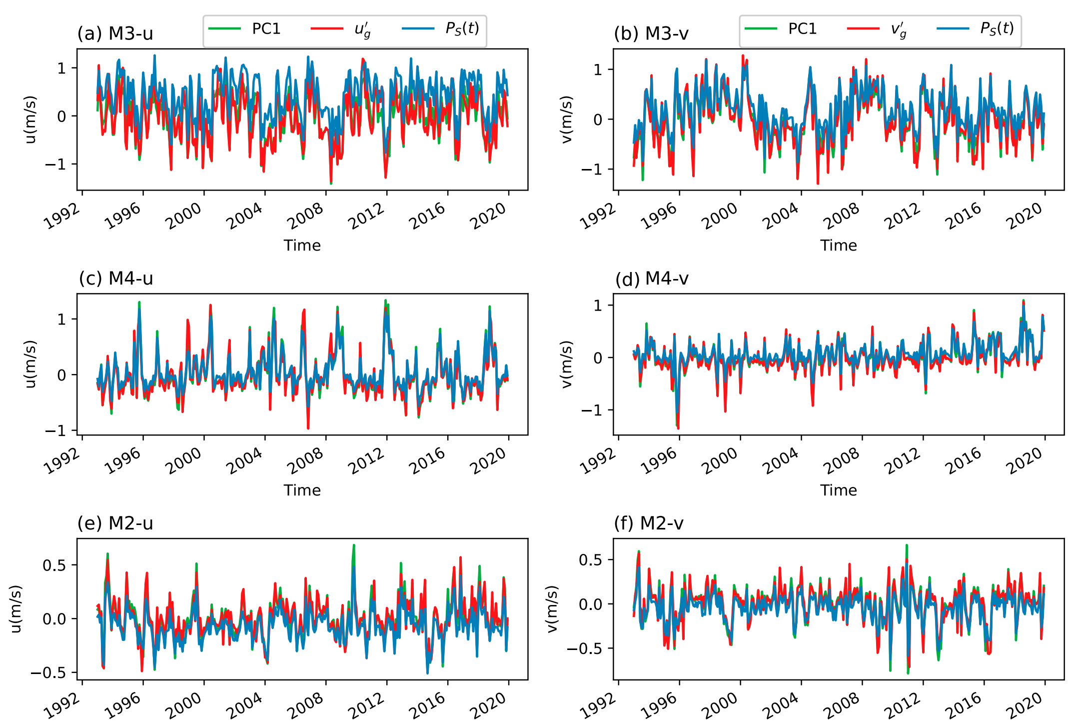

FIG. 7. As in Fig. 5, but for the analysis of OFES data.

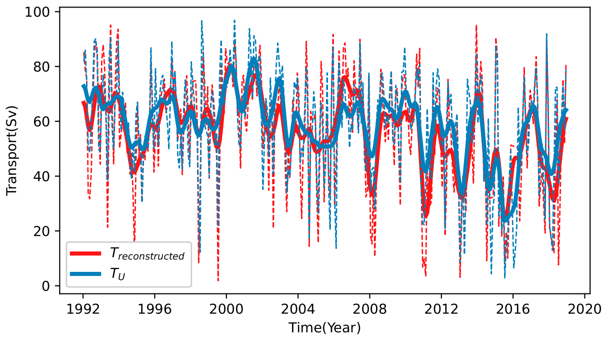

FIG. 8. Cross-sectional transport from M1 to M2 using OFES-derived velocity (blue) and reconstructed velocity (red). The dashed lines denote the monthly mean, and the solid lines denote the low-pass-filtered transport with a 13-month cutoff.

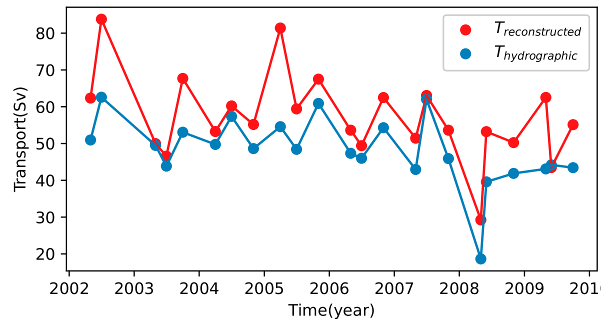

FIG. 9. The volume transport across the 147°E line based on hydrographic data (blue) and the reconstructed method (red).

consistent with the estimated transport of 56.0 Sv. As for the temporal variability, the correlation between these transport time series is 0.88 above 95% significance. Hence, we can confidently conclude that the KE transport can be well estimated based on reconstructed velocity using the EOF and vertical normal mode decomposition. To validate the reconstructed transport, we examined the link between the KE transport and the Pacific decadal oscillation (PDO), which has a strong connection to the KE. Our analysis revealed that the KE transport lags the PDO by 5 years, with a correlation coefficient of 0.68. This result is consistent with previous studies (e.g., Qiu 2003; Andres et al. 2009).

b. Comparison with observations

Next, we compared the estimated transport with in situ observations to test the applicability of this reconstructed method in the real ocean. Considering that the proposed method is a little bit sensitive to ageostrophic motions, we only used monthly mean surface geostrophic velocity from AVISO to smooth out small-scale motions with high-frequency variabilities. In addition to providing stratification to facilitate the mode decomposition, the *T*/*S* data from *WOA18* are also used to set up the geostrophic velocity by using the thermal-wind equation, under the zero-velocity assumption at the bottom. Therefore, the mean transport is calculated using the geostrophic velocity derived from the *WOA18* in situ data.

Notice that the vertical normal mode decomposition proposed here is highly sensitive to bottom topography, and the Kuroshio can extend to the ocean floor in some coastal regions. Under such circumstances, the horizontal velocity in the lower layer is nonnegligible, and the relationship would no longer hold. Here we only selected a decadal-long repeated hydrological section that is away from the coastal region for comparison, despite that there are several repeated sections that have calculated the volume transport in the KE region. Based on repeated hydrographic observations from the Japan Meteorological Agency (JMA), Long et al. (2019) calculated the geostrophic velocity along the 147°E line from 2002 to 2010. Across this section, the mean observed volume transport with a corresponding standard deviation is 48.2 ± 9.0 Sv, and the estimated value is 57.2 + 11.3 Sv, slightly stronger than observations. The RMS difference between the two transport methods is 11 Sv. Additionally, the amplitude of the estimated transport, at 54.5 Sv, is also stronger than the hydrographic-based transport of 44.0 Sv. Despite the difference in their mean intensities, the temporal variability of the estimated transport is in reasonable agreement with observations. As shown in Fig. 9, the time series of estimated transport captures the main feature of observed transport, exhibiting a high correlation reaching up to 0.8 above 95% significance.

In addition to geostrophic calculation from hydrographic data, the KE transport has also been directly measured by current meters in previous studies. For example, Jayne et al. (2009) used combined observations from the KESS to estimate the strength and structure of KE and its recirculation. Based on the Eulerian average, they estimated the KE transport of 79.0 Sv. We also estimated the KE transport across the mooring line of KESS based on the proposed method, and suggest an average transport of 85.3 + 17.5 Sv during the KESS period, which is well in agreement with observations.

5. Summary and discussion

In this study, we have investigated the vertical structure of the horizontal velocity in the Kuroshio Extension region using a mooring array, which is dominated by the barotropic and first baroclinic modes. Meanwhile, this structure is also well reproduced by EOF decomposition, where the EOF1 contains mixed signals from multivertical normal modes. The moored velocities show that the two mode decomposition methods are closely related in the KE regions. Based on these moored measurements, we propose a new method of estimating KE transport by combining the vertical normal modes and EOF1.

For the vertical normal mode decomposition, the first baroclinic mode contributes most to the full velocity, which is surface intensified and reverses in the deep layer with a zero-crossing depth range from 1500 to 1800 m as latitude increases. The depth-independent barotropic mode is also very important, which strengthens the upper-layer flow and weakens the lower-layer flow of the first baroclinic mode. For the EOF decomposition, the EOF1 also drops from the surface to the deep ocean but does not reverse, which contains a mixed signal of barotropic and first baroclinic modes. Since the barotropic and first baroclinic modes tend to cancel each other at the bottom, we could obtain a superimposed vertical mode [$C_s(z)$] by linearly summing up these two modes. After normalizing these two modes to 1 at the surface, we obtained identical projection coefficients, which can be approximated by the surface geostrophic current flow. The EOF1, superimposed vertical mode, and the surface geostrophic velocity are reasonably in agreement with one another.

Therefore, we can reconstruct the vertical profile of the horizontal velocity by combining the surface geostrophic current and the hydrographic data and estimate the KE transport. This method is further tested in the OFES datasets and compared with historical observation. The result is generally in agreement with the OFES output and observation, indicating good adaptability in estimating the KE transport. One major advantage of this method is that it uses only satellite-observed SSH and *WOA18* hydrographic data to estimate the KE volume transport. This volume transport provides a dynamic basis for estimating the mass, momentum, and heat transport of KE, which is crucial for studying the climate impacts of KE.

It should be noted that the projection coefficient is weaker than the surface geostrophic current for some strong currents. A detailed check showed that the vertical structure will be affected by nonlocal eddies or the swinging KE axis. These processes will bring water mass with different hydrographic information, which contaminates the local vertical structure. Despite improvements benefiting from using time-dependent *T*/*S* data, there are still some peaks with tiny differences. This is because the reconstructed method is based on surface geostrophic flow, which will be broken by centrifugal force or nonlinear terms, especially for strong eddies. For example, based on lowered ADCP data, Yoshikawa et al. (2004) showed that the eastward KE transport was 163 Sv across 146°25′E in May 2001 and 113 Sv across 152°30′E in July 2000, which is stronger than our estimation (97 and 94 Sv). We attribute the large disparity to a great amount of nongeostrophic motions as observed by lowered ADCP observations, while the surface velocity from altimeters is basically geostrophic. Fortunately, the potential impact of eddy and swing-axis effects can be minimized by focusing on low-frequency variability and covering the axis in the transport integral. Besides, the vertical normal mode decomposition highly depends on the vertical boundary condition ($w = 0$ at the surface and bottom), making it less effective in the coastal region. Nevertheless, this reconstructed method could well reproduce the low-frequency variabilities of the KE transport in the open ocean.

Acknowledgments. This research is financially supported by the National Natural Science Foundation of China (42225601, 42076009, and 42176006), and Fundamental Research Funds for the Central Universities (202072001 and 202241006). Author Z. Chen is partly supported by the Taishan Scholar Funds (tsqn201812022).

Data availability statement. The mooring data are available at the Kuroshio Extension Mooring System website (https://cn-kems.net/Data/data.zip.001; https://cn-kems.net/Data/data.zip.002). The AVISO data (https://sso.altimetry.fr/) and *World Ocean Atlas 2018* (*WOA18*) data (https://www.ncei.noaa.gov/archive/accession/NCEI-WOA18) are available online. The OFES data were downloaded from the University of Hawai‘i website (https://apdrc.soest.hawaii.edu/datadoc/ofes/ofes.php). Hydrographic data from the 147°E section were downloaded from the Japan Meteorological Agency website (http://www.data.jma.go.jp/gmd/kaiyou/db/vessel_obs/data-report/html/ship/ship.php).

APPENDIX A

The Influence of Remoting Eddies

To investigate the influence of strong currents on local mode decomposition, we have checked the detailed source of these strong currents. It is noteworthy that two strong eddies break the consistency between mode estimation and mooring observation in 2020, where the observed velocity is a little stronger than the mode estimation (Fig. 2). We have tracked these two strong eddies to their generation position. It is found that these two eddies are generated away from the M1 site (Fig. A1); not surprisingly, they will bring water columns that are quite different from local seawater. The local hydrographic information is inconsistent with nonlocal eddies, and therefore, the mode decomposition will lose its adaptability to these currents.

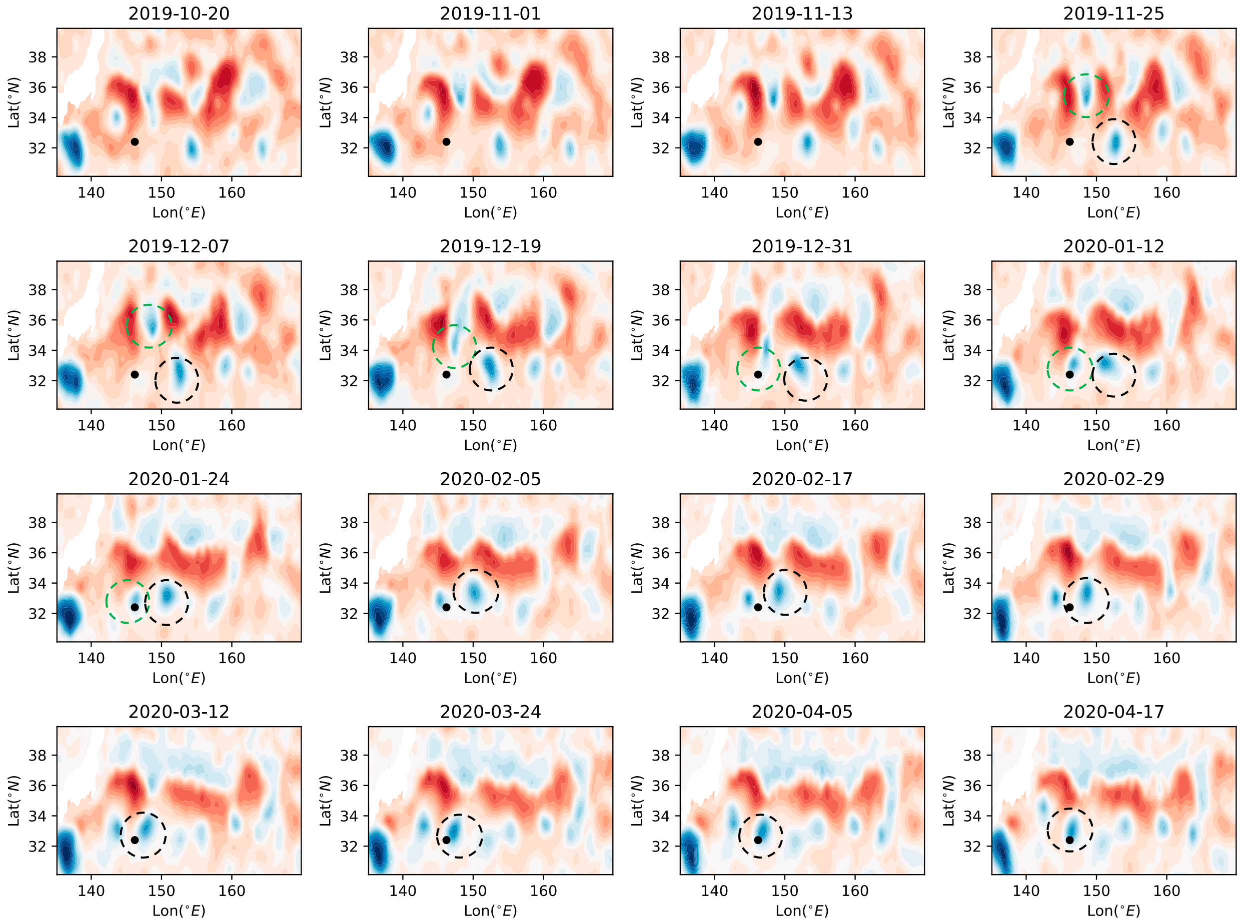

FIG. A1. The sea surface height anomaly in the KE region from October 2019 to April 2020 (color shading). The black dot represents the M1 site. The two circles mark the position of two strong eddies that cause the peak difference in Figs. 2 and 3. The green circle denotes the eddy that comes from a high latitude, and the black circle denotes the eddy that comes from downstream of the KE.

APPENDIX B

Vertical Mode Decomposition Based on Observed Temperature

Here we also used the moored temperature from M1 to calculate the ocean stratification and further conduct mode decomposition, whereas the salinity data are still from the WOA dataset (Fig. B1). The results are similar to the mode decomposition purely based on the WOA *T*/*S*. Despite the hydrographic difference between observed data and climatological data, the basic vertical structure is still dominated by the barotropic and the first baroclinic modes.

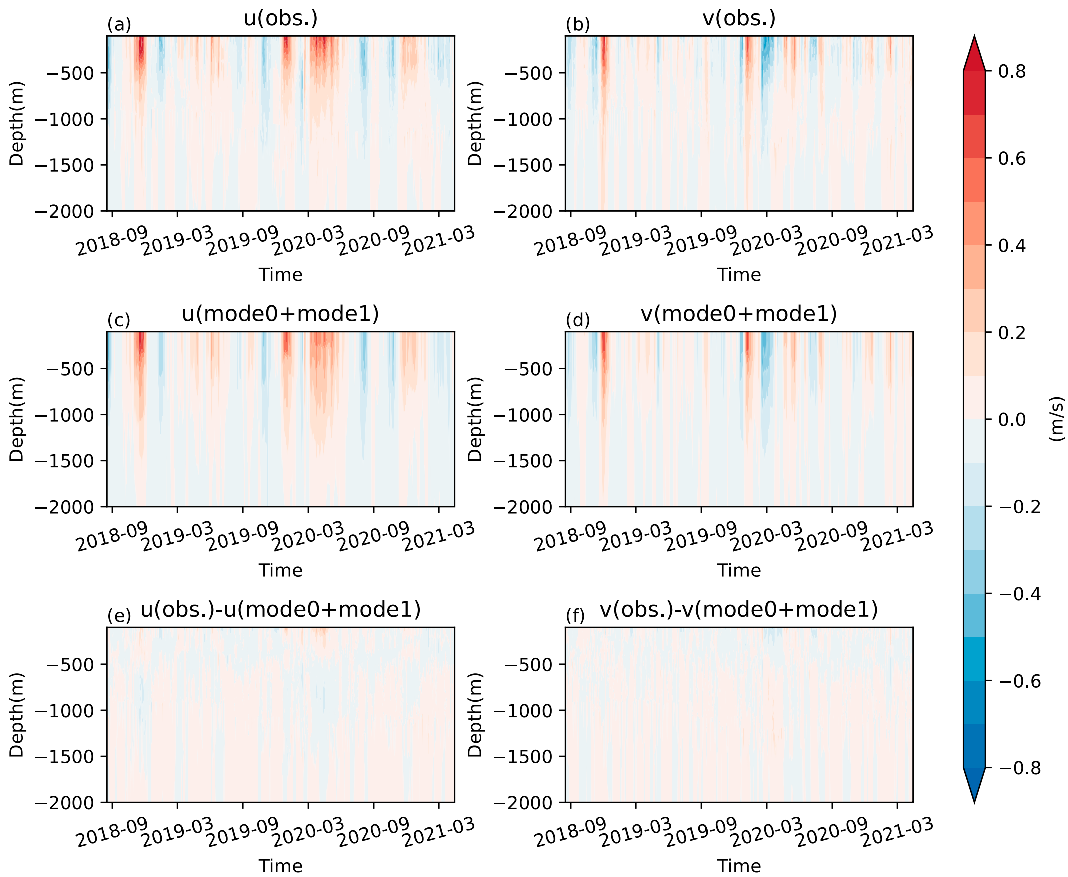

FIG. B1. As in Fig. 2, but the moored temperature is used to calculate the ocean stratification.

REFERENCES

Andres, M., J.-H. Park, M. Wimbush, X.-H. Zhu, H. Nakamura, K. Kim, and K. I. Chang, 2009: Manifestation of the Pacific decadal oscillation in the Kuroshio. *Geophys. Res. Lett.*, **36**, L16602, https://doi.org/10.1029/2009GL039216.

Bishop, S. P., D. R. Watts, J.-H. Park, and N. G. Hogg, 2012: Evidence of bottom-trapped currents in the Kuroshio Extension region. *J. Phys. Oceanogr.*, **42**, 321–328, https://doi.org/10.1175/JPO-D-11-0144.1.

Chelton, D. B., R. A. DeSzoeke, M. G. Schlax, K. El Naggar, and N. Siwertz, 1998: Geographical variability of the first baroclinic Rossby radius of deformation. *J. Phys. Oceanogr.*, **28**, 433–460, https://doi.org/10.1175/1520-0485(1998)028<0433:GVOTFB>2.0.CO;2.

Ducet, N., P. Y. Le Traon, and G. Reverdin, 2000: Global high-resolution mapping of ocean circulation from TOPEX/Poseidon and ERS-1 and -2. *J. Geophys. Res.*, **105**, 19 477–19 498, https://doi.org/10.1029/2000JC900063.

Hall, M. M., 1989: Velocity and transport structure of the Kuroshio Extension at 35°N, 152°E. *J. Geophys. Res.*, **94**, 14 445–14 459, https://doi.org/10.1029/JC094iC10p14445.

Hannachi, A., I. T. Jolliffe, and D. B. Stephenson, 2007: Empirical orthogonal functions and related techniques in atmospheric science: A review. *Int. J. Climatol.*, **27**, 1119–1152, https://doi.org/10.1002/joc.1499.

Hiroe, Y., I. Yasuda, K. Komatsu, K. Kawasaki, T. M. Joyce, and F. Bahr, 2002: Transport of North Pacific Intermediate Water in the Kuroshio–Oyashio interfrontal zone. *Deep-Sea Res. II*, **49**, 5353–5364, https://doi.org/10.1016/S0967-0645(02)00195-9.

Hurlburt, H. E., A. J. Wallcraft, W. J. Schmitz Jr., P. J. Hogan, and E. J. Metzger, 1996: Dynamics of the Kuroshio/Oyashio Current system using eddy-resolving models of the North Pacific Ocean. *J. Geophys. Res.*, **101**, 941–976, https://doi.org/10.1029/95JC01674.

Itoh, S., and I. Yasuda, 2010: Characteristics of mesoscale eddies in the Kuroshio–Oyashio Extension region detected from the distribution of the sea surface height anomaly. *J. Phys. Oceanogr.*, **40**, 1018–1034, https://doi.org/10.1175/2009JPO4265.1.

Jayne, S. R., and Coauthors, 2009: The Kuroshio Extension and its recirculation gyres. *Deep-Sea Res. I*, **56**, 2088–2099, https://doi.org/10.1016/j.dsr.2009.08.006.

Ji, J., C. Dong, B. Zhang, Y. Liu, B. Zou, G. P. King, G. Xu, and D. Chen, 2018: Oceanic eddy characteristics and generation mechanisms in the Kuroshio Extension region. *J. Geophys. Res. Oceans*, **123**, 8548–8567, https://doi.org/10.1029/2018JC014196.

Joyce, T. M., 1987: Hydrographic sections across the Kuroshio Extension at 165°E and 175°W. *Deep-Sea Res.*, **34A**, 1331–1352, https://doi.org/10.1016/0198-0149(87)90130-0.

Kalnay, E., and Coauthors, 1996: The NCEP/NCAR 40-Year Reanalysis Project. *Bull. Amer. Meteor. Soc.*, **77**, 437–471, https://doi.org/10.1175/1520-0477(1996)077<0437:TNYRP>2.0.CO;2.

Kida, S., and Coauthors, 2015: Oceanic fronts and jets around Japan: A review. *J. Oceanogr.*, **71**, 469–497, https://doi.org/10.1007/s10872-015-0283-7.

Locarnini, R. A., and Coauthors, 2019: *Temperature*. Vol. 1, *World Ocean Atlas 2018*, NOAA Atlas NESDIS 81, 52 pp.

Long, Y., X.-H. Zhu, X. Guo, and H. Huang, 2018: Temporal variation of Kuroshio nutrient stream south of Japan. *J. Geophys. Res. Oceans*, **123**, 7896–7913, https://doi.org/10.1029/2017JC013635.

——, ——, and ——, 2019: The Oyashio nutrient stream and its nutrient transport to the mixed water region. *Geophys. Res. Lett.*, **46**, 1513–1520, https://doi.org/10.1029/2018GL081497.

Ma, J., S. Hu, D. Hu, C. Villanoy, Q. Wang, X. Lu, and X. Yuan, 2022: Structure and variability of the Kuroshio and Luzon Undercurrent observed by a mooring array. *J. Geophys. Res. Oceans*, **127**, e2021JC017754, https://doi.org/10.1029/2021JC017754.

Ma, X., and Coauthors, 2016: Western boundary currents regulated by interaction between ocean eddies and the atmosphere. *Nature*, **535**, 533–537, https://doi.org/10.1038/nature18640.

Masumoto, Y., and Coauthors, 2004: A fifty-year eddy-resolving simulation of the World Ocean—Preliminary outcomes of OFES (OGCM For the Earth Simulator). *J. Earth Simul.*, **1**, 35–56.

Oliver, E. C. J., J. A. Benthuysen, S. Darmaraki, M. G. Donat, A. J. Hobday, N. J. Holbrook, R. W. Schlegel, and A. Sen Gupta, 2021: Marine heatwaves. *Annu. Rev. Mar. Sci.*, **13**, 313–342, https://doi.org/10.1146/annurev-marine-032720-095144.

Qiu, B., 2003: Kuroshio Extension variability and forcing of the Pacific decadal oscillations: Responses and potential feedback. *J. Phys. Oceanogr.*, **33**, 2465–2482, https://doi.org/10.1175/2459.1.

——, and S. Chen, 2005: Variability of the Kuroshio Extension jet, recirculation gyre, and mesoscale eddies on decadal time scales. *J. Phys. Oceanogr.*, **35**, 2090–2103, https://doi.org/10.1175/JPO2807.1.

——, ——, and P. Hacker, 2007: Effect of mesoscale eddies on subtropical mode water variability from the Kuroshio Extension System Study (KESS). *J. Phys. Oceanogr.*, **37**, 982–1000, https://doi.org/10.1175/JPO3097.1.

Ren, Q., Y. Li, F. Wang, L. Song, C. Liu, and F. Zhai, 2018: Seasonality of the Mindanao Current/Undercurrent system. *J. Geophys. Res. Oceans*, **123**, 1105–1122, https://doi.org/10.1002/2017JC013474.

Suga, T., and K. Hanawa, 1995: The subtropical mode water circulation in the North Pacific. *J. Phys. Oceanogr.*, **25**, 958–970, https://doi.org/10.1175/1520-0485(1995)025<0958:TSMWCI>2.0.CO;2.

Tsunogai, S., T. Ono, and S. Watanabe, 1993: Increase in total carbonate in the western North Pacific water and a hypothesis on the missing sink of anthropogenic carbon. *J. Oceanogr.*, **49**, 305–315, https://doi.org/10.1007/BF02269568.

Uchida, H., S. Imawaki, and J. H. Hu, 1998: Comparison of Kuroshio surface velocities derived from satellite altimeter and drifting buoy data. *J. Oceanogr.*, **54**, 115–122, https://doi.org/10.1007/BF02744385.

Vallis, G. K., 2017: *Atmospheric and Oceanic Fluid Dynamics: Fundamentals and Large-Scale Circulation.* 2nd ed. Cambridge University Press, 946 pp.

Yang, Y., and X. S. Liang, 2018: On the seasonal eddy variability in the Kuroshio Extension. *J. Phys. Oceanogr.*, **48**, 1675–1689, https://doi.org/10.1175/JPO-D-18-0058.1.

——, ——, and H. Sasaki, 2021: Vertical coupling and dynamical source for the intraseasonal variability in the deep Kuroshio Extension. *Ocean Dyn.*, **71**, 1069–1086, https://doi.org/10.1007/s10236-021-01482-9.

Yoshikawa, Y., J. A. Church, H. Uchida, and N. J. White, 2004: Near bottom currents and their relation to the transport in the Kuroshio Extension. *Geophys. Res. Lett.*, **31**, L16309, https://doi.org/10.1029/2004GL020068.

Zhu, R., Z. Chen, Z. Zhang, H. Yang, and L. Wu, 2021: Subthermocline eddies in the Kuroshio Extension region observed by mooring arrays. *J. Phys. Oceanogr.*, **51**, 439–455, https://doi.org/10.1175/JPO-D-20-0047.1.

Zweng, M. M., and Coauthors, 2019: *Salinity*. Vol. 2, *World Ocean Atlas 2018*, NOAA Atlas NESDIS 82, 50 pp.